

# Laser-driven plasmonic gratings for multiple images hiding

N. Sharma<sup>a</sup>, M. Vangheluwe<sup>b</sup>, F. Vocanson<sup>a</sup>, A. Cazier<sup>a</sup>, M. Bugnet<sup>c</sup>, S. Reynaud<sup>a</sup>, A. Vermeulin<sup>b</sup>, N. Destouches<sup>a\*</sup>

<sup>a</sup> *Univ Lyon, UJM-Saint-Etienne, CNRS, Institut d'Optique Graduate School, Laboratoire Hubert Curien UMR 5516, F-42023, Saint-Etienne, France*

<sup>b</sup> *HID Global CID, 92150 Suresnes, France*

<sup>c</sup> *University of Lyon, INSA-Lyon, UCBL Lyon 1, MATEIS, UMR 5510 CNRS, Villeurbanne Cedex, France*

## 1- Influence of the laser fluence and scan speed on the film nanostructures.

This section explains how the sketch of Figure 1 in the main paper was drawn and provides new information about the nanoparticles size and density.

SEM images of Figure S1 illustrate the changes in the film morphology on plastic substrate after laser processing with different scan speeds and fluences at 25 kHz laser repetition rate. At a fluence of 124 mJ/cm<sup>2</sup> (Figure S1 c), and slow scan speed of 1.8 mm/s, few Ag nanoparticles in the form of nanorods are observed on the surface where no grating is formed, but most of silver nanoparticles are embedded in the film as attested by the irregular contrast of the SEM image of the surface that is characteristic of the presence of a high density of Ag nanoparticles (brighter contrast) just below the film surface. Because of the low contrast and the blurred outline of the nanoparticles, SEM images are not suitable to properly measure the size distribution and the nanoparticle density. We can however estimate that nanoparticle sizes between 10 and 40 nm are present in the film. Such a film does not delaminate from the substrate. When increasing the scan speed to 3.08 mm/s at the same fluence, Ag nanoparticles are still few on the film surface and they have a rather circular shape; A high density of Ag nanoparticles is still present below the surface with a size that does not exceed 25 nm, as estimated from SEM images. A slight periodic contrast is now observed on the SEM images corresponding to the presence of LIPSS with a low amplitude. The film does not delaminate. At a scan speed of 10.5 mm/s, the nanoparticles on the film surface are rare and with a circular shape. Embedded nanoparticles have a lower size than in the previous case and are difficult to identify by SEM. Surface gratings can be distinguished but with less contrast than at the previous speed. They have been highlighted by white double dash lines when they exist. At a higher fluence of 159 mJ/cm<sup>2</sup> (Figure S1b), spallation (shown in inset when imaging samples at a lower magnification) occurs at 1.8 mm/s and LIPSS start emerging when increasing the scan speed. Most of the nanoparticles are embedded and difficult to identify

from SEM. At the fluence of 195 mJ/cm<sup>2</sup> (Figure S1a), the spallation is present over a larger speed range and more contrasted LIPSS occur at the highest scan speed of 10.5 mm/s.

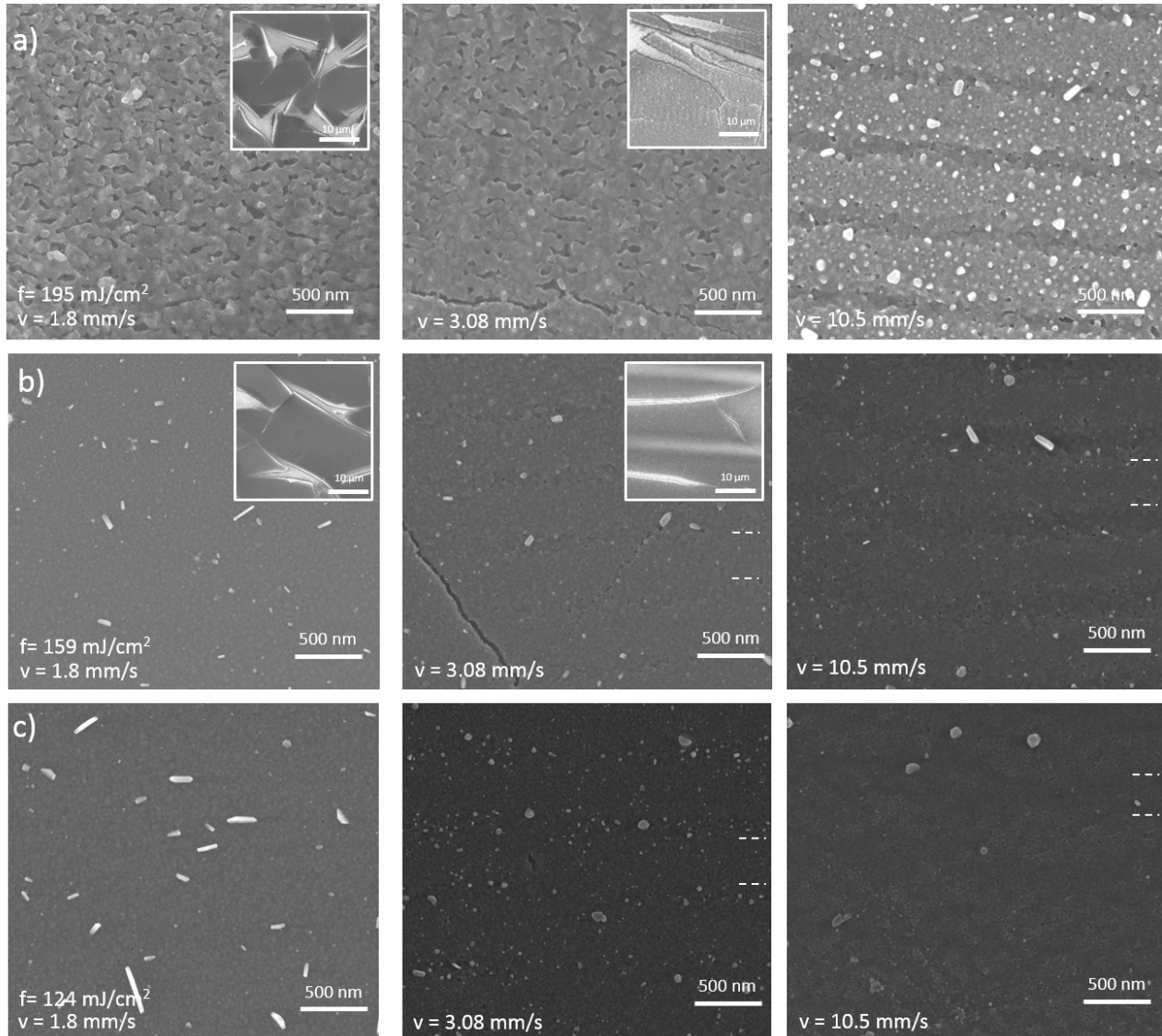


**Figure S1:** SEM images showing the morphological changes in the nanocomposite TiO<sub>2</sub>:Ag film after laser processing (25 kHz, 515 nm) for three different fluences of a) 124, b) 159 and c) 195 mJ/cm<sup>2</sup> and for three different scan speeds of 1.8, 3.08 and 10.5 mm/s. Low magnification images in inset show the film spallation that occurs on some samples.

The presence of LIPSS on the sample surface was better identified when observing diffraction of white light on the sample. Figure S2 shows photographs of a sample, where squares were drawn with varying scan speeds and fluences, taken under right conditions of observation and illumination to catch optical diffraction of blue, green and yellow radiations. The diffraction efficiency qualitatively decreases when decreasing the speed and the fluence, except for the two lowest fluences where the maximum speed also leads to low diffraction. Such information together with SEM observations was used to draw the sketch of Figure 1 in the main text.

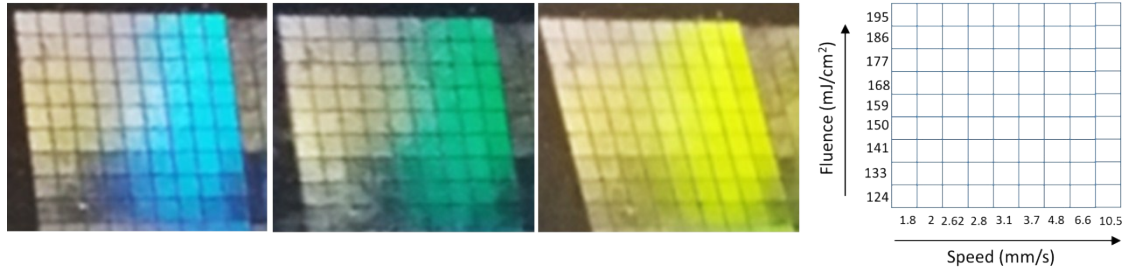


**Figure S2:** Diffraction by LIPSS patterns on plastic substrate. Photographs of a sample taken under white light and different angles of observation to qualitatively highlight the variations in the diffraction efficiency with the scan speed and laser fluence. Squares are 3 mm wide.

Additional TEM characterizations were carried out to better investigate the influence of the fluence and speed on the nanoparticle size and density. Two series of samples were initially prepared by FIB, from squares drawn on a plastic substrate and on a glass substrate. For experimental reasons only one lamella from the plastic substrate was observable and was reported in Figure 2 of the main text. Three other samples produced on glass were observed and allow to inform about the effect of fluence on the nanoparticle size and density at low speed. As already observed from SEM images, Ag nanoparticles mainly grow inside the TiO<sub>2</sub> film rather than on the film surface and TEM characterizations (Figure S3) on cross-sections confirm the high density of embedded particles at low fluence. At increasing fluence, bigger nanoparticles grow in the top part of the film leading to a lower nanoparticle density and to a double peak size distribution. The size of the biggest particles increases with the laser fluence while the smallest nanoparticles seem to shrink with the laser fluence.

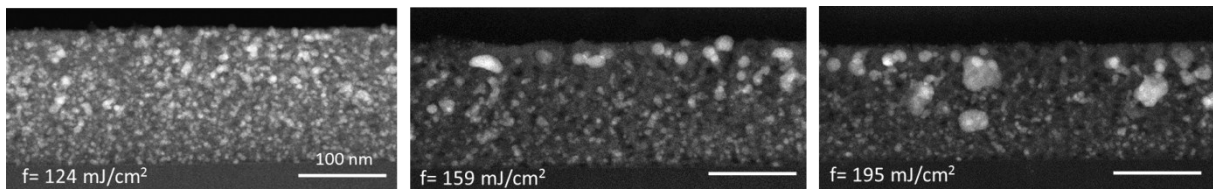


**Figure S3:** TEM images showing the influence of the laser fluence on the nanoparticle growth, with a scan speed of 1.8 mm/s on glass substrate. The scale bar is 100 nm in each image.

## 2- Observation conditions of the hidden images

When illuminating a grating of period  $\Lambda$  with a collimated beam under the incidence angle  $\theta_i$  in the plane perpendicular to the grating lines, diffraction takes place in the plane of incidence under

the angle  $\theta_p$  defined by the grating equation:  $\sin(\theta_p) = -\sin(\theta_i) + p\frac{\lambda}{\Lambda}$ . When rotating the grating in its plane, i.e. introducing an azimuthal angle between the plane of incidence and the perpendicular to the grating lines, conical diffraction occurs and the diffracted orders do not belong anymore to the plane of incidence. So, continuously varying the grating orientation in an angular range from 0° to 15° allows tuning the intensity of diffracted light that can be captured by a camera located in the plane of incidence from a maximum value to zero (Figure S4).

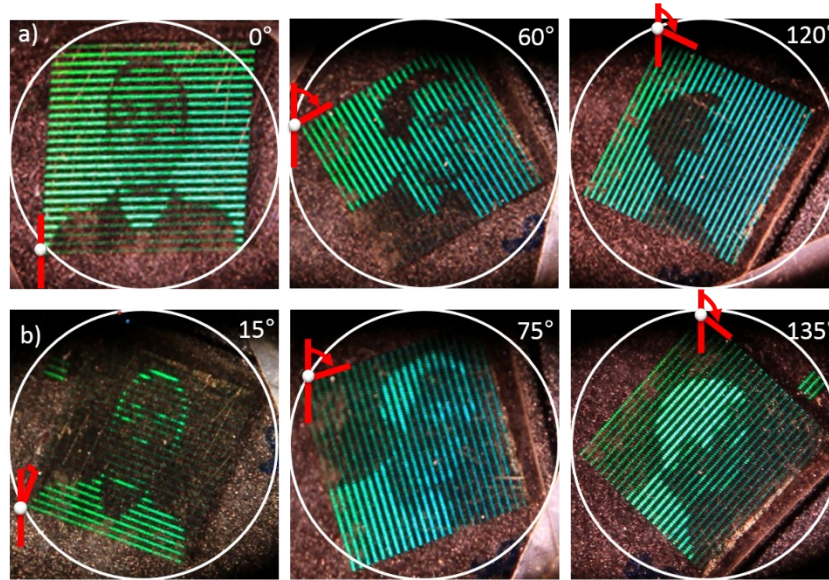


**Figure S4: Multiple image hiding on polycarbonate substrate.** Interlaced diffractive images at azimuthal angles of a)  $0^\circ$ ,  $60^\circ$  and  $120^\circ$  as shown in the paper with their respective b) negative images at  $15^\circ$ ,  $75^\circ$  and  $135^\circ$  angles.

When working with nanocomposite films coated on glass substrate, higher resolution images can be printed. Two illustrations are provided in Figure S5 and S6.

Figure S3a shows a sketch of the setup used to image in the plane of incidence the different interlaced raster pictures printed in a single image. The angle between the light source and the camera is fixed at  $35^\circ$ . A rotation of the sample changes both the incidence angle  $\theta_i$  and the angle  $\theta_1$  of the first diffracted order imaged on the camera. These angles are linked as follows:

$$\theta_1 = \theta_i - 35^\circ \quad (\text{EqS1})$$

Also knowing the period of the self-organized grating ( $\Lambda = 495 \text{ nm}$ ), one can deduce the wavelength at which the image is recorded on the camera. It is given by the grating equation according to equation EqS2:

$$\lambda = \Lambda (\sin \theta_i + \sin \theta_1) \quad (\text{EqS2})$$

Figure S5b gives 5 pictures recorded at different angles of incidence with the corresponding diffraction angles and wavelengths. In Figure S5c, we show the three interlaced images and their negative images recorded for a fixed angle of incidence of  $55.5^\circ$  when rotating the sample in its plane, i.e. when varying the azimuthal angle from  $0^\circ$  to  $135^\circ$ .

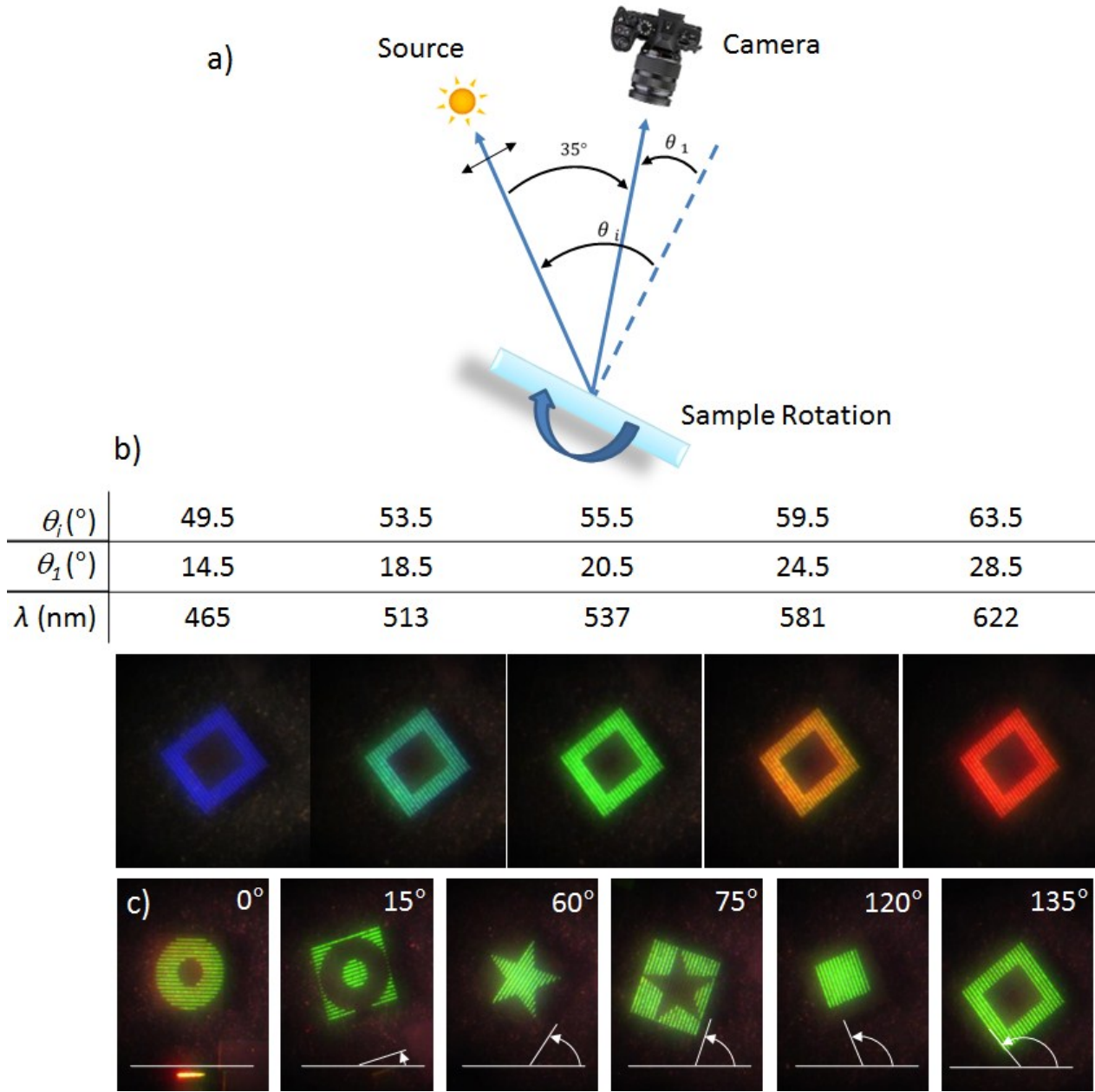


**Figure S5: Another illustration of hidden multiple image printing on glass substrate** a) Setup used for recording pictures in the plane of incidence b) Tabulated values for  $\theta_i$ ,  $\theta_1$  and respective  $\lambda$  as calculated using equations EqS1 and EqS2, followed by images taken for these angles c) Photographs of the three images hidden in this sample recorded at azimuthal angles of  $0^{\circ}$ ,  $60^{\circ}$  and  $120^{\circ}$  with their respective negative images at  $15^{\circ}$ ,  $75^{\circ}$  and  $135^{\circ}$  angles with angle of incidence and diffraction fixed at  $55.5^{\circ}$  and  $20.5^{\circ}$ , respectively.

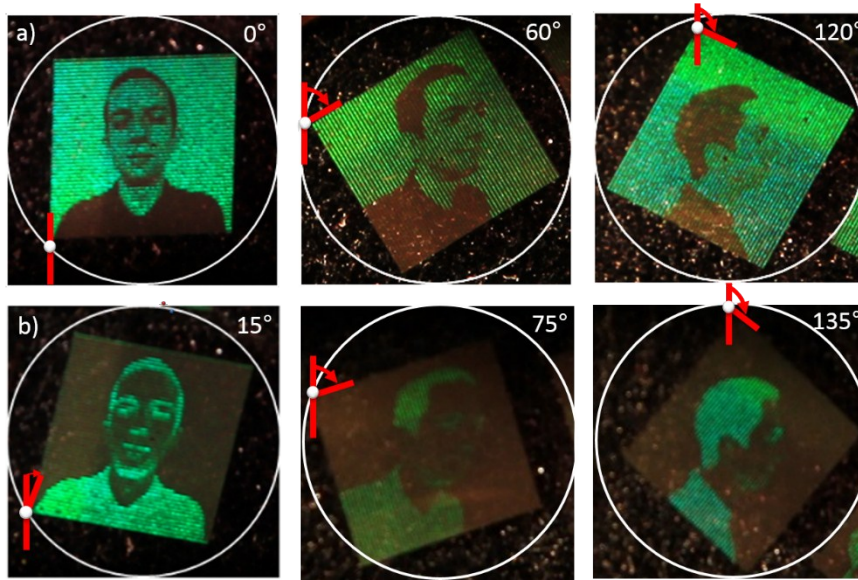


**Figure S6: Multiple image hiding on glass substrate.** Interlaced diffractive images with same human portrait as in Figure S1 and a better resolution of  $40\ \mu\text{m}$ . Azimuthal angles a)  $0^\circ$ ,  $60^\circ$  and  $120^\circ$  displays the three positive images while their respective negative images are shown in b) at  $15^\circ$ ,  $75^\circ$  and  $135^\circ$  angles.

### 3- Film at the pixel size

Pixels are illustrated in Figure S7 for the image printed on the plastic substrate. Each pixel is a square of size  $160^2\ \mu\text{m}^2$  made of four laser lines written with a fixed polarization angle. Figure S7a, shows the diffractive image along with an image of lines recorded with an optical microscope. The dashed lines in the following image illustrate the size of one pixel. On plastic sample, because of the acceleration and deceleration of the scan speed, spallation occurs at line edges as shown by SEM (Fig. S7b) where the two bright areas correspond to the starting point of two adjacent lines. These areas appear dark on the optical microscopy image recorded in reflection in Fig. S7a. Another SEM image with an intermediate magnification is provided in Figure S7c to show the last magnification at which LIPSS are perceptible.

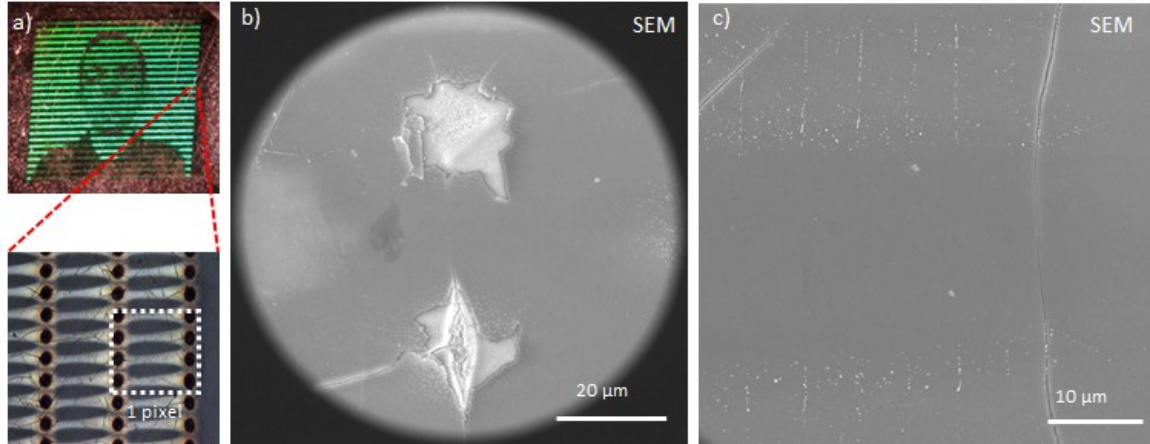


**Figure S7:** Illustration of the pixelated printing on plastic substrate. a) Diffractive image with an optical microscopy image showing the size of a pixel (white dashed square), made of four laser lines. b) A low magnification SEM image showing the starting point of two adjacent laser lines (black dot in the optical microscopy image in a). c) LIPSS formation for two different laser lines from a single pixel. The contrast of the LIPSS from a lower magnification is weak, illustrating that a single pixel and LIPSS grating can't be observed together in a single image.

Drawing images pixel by pixel using a laser scanning process, as described in the article, is made with a home-made Labview software that stops the translation stage between each pixel to let time for the motorized rotation stage controlling the half-wave plate to reach the targeted laser polarization. During this waiting time, the accumulation of laser pulses is much higher than what is expected inside the laser line, and leads to a film damage on the plastic substrate, which is not really perceptible when working on a glass substrate. Each laser line is then affected by dark points at its ends that do not diffract light, as shown in Figure S7. This effect forces to increase the laser line length to  $160\ \mu\text{m}$  to get a significant diffracting length. And in order to maintain square pixels, four lines  $40\ \mu\text{m}$  apart from each other were used for each pixel.

An improvement in the image resolution could be done by modifying the Labview software and the setup itself. In order to work at the highest possible resolution, the laser drawing could be done dot by dot by controlling the number of pulses per dot rather than the scan speed, but this would require adding a pulse picker to the setup. In such a case, the resolution would be defined by the beam size on the sample surface, which could be decreased to few micrometers in order to optimize the resolution. The limit would then be the minimum size required to observe the formation of LIPSS. One has however to note that LIPSS formed along lines are usually more regular than LIPSS formed in dots. And the diffraction efficiency of each dot is directly correlated to the regularity of the grating. Accordingly, optimizing the writing process in terms of diffraction efficiency may be less efficient with a dot matrix printing.

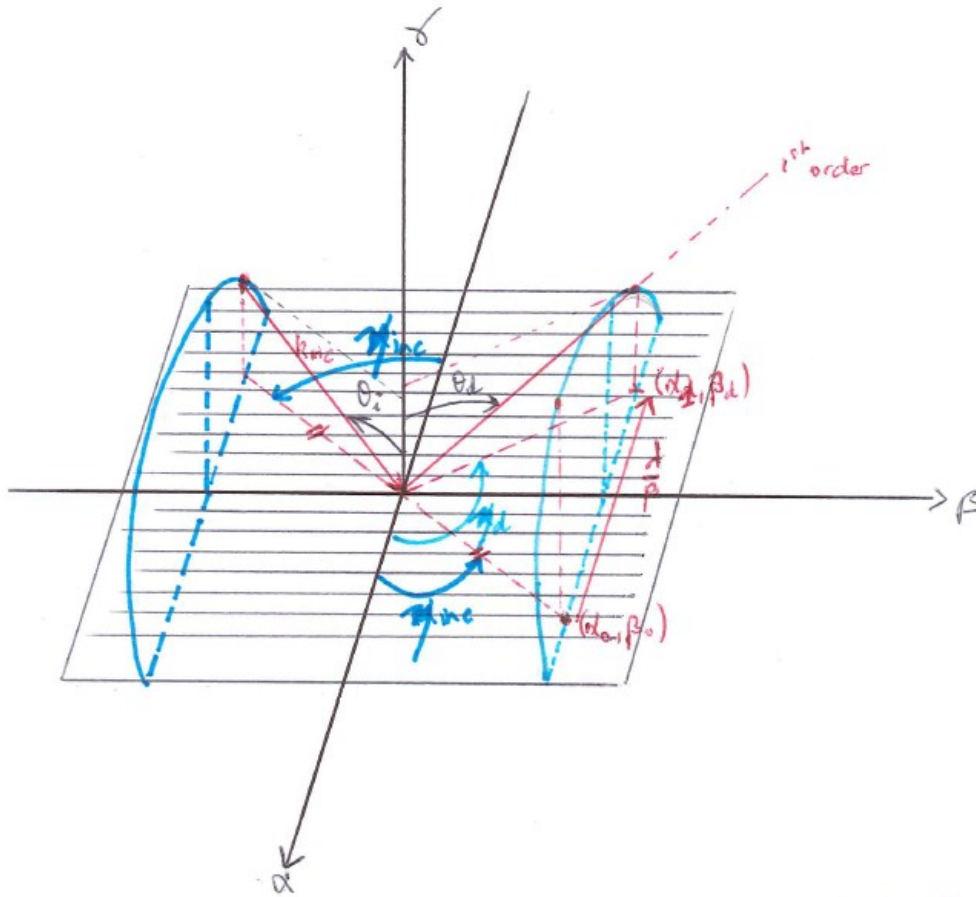
#### 4- Note concerning the pixel brightness

The brightness of a pixel depends on the conditions of observation and illumination that will be implemented by the user. The objective was not to reach a specified value for the brightness but rather to allow the identification of independent images. This note aims at giving some clues about the parameters that govern the pixel brightness and the optimization of encoding parameters.

For the sake of simplicity, we assume that each pixel contains exactly the same perfectly regular grating (no defect in the self-organization process) but tilted by a certain angle  $A$  in the sample plane. Let us consider a single pixel characterized by the grating orientation  $A$  illuminated with a perfectly collimated beam along the direction defined by the azimuthal angle  $\eta_{inc} = A$  and the polar angle  $\theta_i$  (as drawn on the sketch below). This corresponds to a case of conical diffraction and the light at wavelength  $\lambda_0$  is diffracted in the direction out of the plane of incidence defined by an azimuthal angle  $\eta_d$  and a polar angle  $\theta_d$  that fulfil the grating equation written along  $\alpha$  and  $\beta$  directions as follows:

**$\alpha$  axis:**  $\sin\theta_{inc}\cos\eta_{inc} \pm \sin\theta_d\cos\eta_d = m\frac{\lambda_0}{P}$ , with  $m = \pm 1, \pm 2 \dots$ , and  $P$  the grating period

**$\beta$  axis:**  $\sin\theta_d\sin\eta_d = \sin\theta_{inc}\sin\eta_{inc}$



As a result, the pixel characterized by the angle  $A$  diffracts light out of the plane of incidence where light is collected by the sensor and it should not be detected as a bright pixel on the

camera. But, the angular width of the diffraction pattern (around the diffraction angle defined above) is not null. It depends on the shape of the grating (which should be the same for each pixel if the self-organization process could produce perfectly reproducible gratings), and also on the angular aperture of the illuminating beam (which depends on the observation conditions implemented by the user to observe the hidden images). The larger the angular width of the diffraction pattern, the brighter the intensity of "pixel A" on the camera. Note that the brightness of "pixel A" also depends on the angular aperture of the used camera.

As the system is thought to be used to display different hidden images, care was taken to make sure that the different images could be observed completely independently. For this we looked for angular ranges where only the pixels from one image (among the three) could light up. This optimization was done in illumination and observation conditions that were not too severe to ensure a proper operation in a broad range of conditions of use (observation with the naked eye under ambient light -sun light or artificial light-). It led us to define angular ranges of a maximum of  $15^\circ$  each  $60^\circ$ . An angular range of  $15^\circ$  is large enough to encode a greyscale within each image. The angular separation of  $60^\circ$  between each image ensures that no pixel from the other images brightens when one image is observed. Note that encoding 4 images within angular ranges of  $7^\circ$  each  $45^\circ$  leads to cross-talking (the images cannot be seen independently of each other).

Another care was given to maximize the diffraction efficiency to ensure an easy observation. This was the objective of the parameter study shown in the first part of the main text and of the supplementary information. And, as the grating profile cannot be controlled independently from the other grating parameters with such a writing technology, the variations in the pixel brightness within the selected angular range were not particularly studied.

Finally, it is worth reminding that the brightness of each pixel depends on the orientation of the sample in its plane and that each pixel will exhibit its higher brightness when its grating orientation will be perpendicular to the plane of incidence defined by the incident light beam and the normal to the sample.